6-13-2012

High CO_2 Permeation Flux Enabled by Highly Interconnected Three-Dimensional Ionic Channels in Selective CO_2 Separation Membranes

Lingling Zhang
University of South Carolina - Columbia, zhang257@email.sc.edu

Nansheng Xu
University of South Carolina - Columbia, xun@cec.sc.edu

Xue Li
University of South Carolina - Columbia, lixue@cec.sc.edu

Siwei Wang

Kevin Huang
University of South Carolina - Columbia, huang46@cec.sc.edu

Publication Info

Published in *Energy & Environmental science*, Volume 5, Issue 8, 2012, pages 8310-8317.

Zhang, L., Xu, N.., Li, X., Wang, S., Huang, K., Harris, W. H., & Chiu, W. K. S. (2012). High CO_2 Permeation Flux Enabled by Highly Interconnected Three-Dimensional Ionic Channels in Selective CO_2 Separation Membranes. Energy & Environmental Science, 5 (8), 8310 - 8317. http://dx.doi.org/10.1039/C2EE22045H

Energy & Environmental Science

Cite this: *Energy Environ. Sci.*, 2012, **5**, 8310

www.rsc.org/ees

PAPER

High CO_2 permeation flux enabled by highly interconnected three-dimensional ionic channels in selective CO_2 separation membranes†

Lingling Zhang,[a] Nansheng Xu,[a] Xue Li,[a] Siwei Wang,[a] Kevin Huang,*[a] William H. Harris[b] and Wilson K. S. Chiu[b]

Received 25th April 2012, Accepted 11th June 2012
DOI: 10.1039/c2ee22045h

Abatement of CO_2 emissions from existing fossil-fueled power plants is currently the sole near-term solution to stabilize CO_2 concentration in the atmosphere. Separation and capture of CO_2 from process streams of these power plants is the first step toward this effort. In this paper, we report a high flux membrane consisting of highly and efficiently interconnected three-dimensional ionic channels prepared from a combined "co-precipitation" and "sacrificial-template" synthesis. The membranes exhibit remarkable CO_2 permeation characteristic, achieving a CO_2 flux density two orders of magnitude higher than other similar systems reported in the literature. The experimental results also have an excellent agreement with the theoretical predictions. Overall, the demonstrated dual-phase membranes show a great promise for selective pre-combustion CO_2 separation.

Introduction

Fossil fuels are the dominant energy source powering our modern society, largely due to their competitive cost and wide accessibility. However, burning fossil fuels emits carbon dioxide (CO_2), a greenhouse gas that can cause climate change and ultimately threaten the survival of humanity. An alarming statistic shows that nearly 40% of 5.8 billion metric tons of the total U.S. anthropogenic CO_2 emissions in 2008 resulted from burning fossil fuels for 71% of the total U.S. electricity generation.[1,2] Effectively mitigating CO_2 emissions from the use of fossil fuels has, therefore, become an intense subject of scientific research as well as political debate in recent years.

There are four general strategies currently being considered for the abatement of CO_2 emissions: demand-side conservation, supply-side efficiency improvement, potential increase in nuclear and renewable energy supplies, and implementation of carbon capture and storage (CCS) technology into existing fossil-fueled power plants.[3,4] Of all the options, CCS is regarded as the sole practical near-term solution to effectively stabilize atmospheric CO_2 concentration.[4]

To realize the ultimate CCS, separation and capture of CO_2 from a CO_2-containing industrial process stream is the first step. The CO_2 capture technologies currently being developed and

[a]*Department of Mechanical Engineering, University of South Carolina, Columbia, SC 29208, USA. E-mail: kevin.huang@sc.edu; Fax: +1-803-777-0137; Tel: +1-803-777-0204*
[b]*Department of Mechanical Engineering, University of Connecticut, Storrs, CT 06269, USA*

† Electronic supplementary information (ESI) available: Description of the carbon formation domain and deduction of modified CO_2 flux equation are included in the ESI. See DOI: 10.1039/c2ee22045h

Broader context

Fossil fuels are the dominant energy source powering our modern society, largely due to their competitive cost and wide accessibility. However, burning fossil fuels emits carbon dioxide (CO_2), a greenhouse gas that can cause climate change and ultimately threaten the survival of humanity. Effective abatement of CO_2 emissions from the use of fossil fuels has become an intense subject of scientific research as well as political debate in recent years. Separation and capture of CO_2 from fossil-fueled power plants is the first step toward stopping CO_2 emissions to the atmosphere. The incumbent CO_2 capture technologies currently being developed and demonstrated for existing fossil-fueled power plants are either too expensive or less efficient/selective. Here, we report a high flux membrane consisting of highly and efficiently interconnected three-dimensional ionic channels prepared from a combined "co-precipitation" and "sacrificial-template" synthesis. The membranes exhibit remarkable CO_2 permeation characteristic: achieving CO_2 flux density two orders of magnitude higher than other similar systems reported in the literature, approaching to the level for commercial use, and agreeing remarkably well with the theoretical model. Overall, the demonstrated dual-phase membranes show a great promise for selective pre-combustion CO_2 separation.

demonstrated for existing fossil-fueled power plants are primarily targeting three different stages: post-combustion, oxyfuel combustion and pre-combustion.[4–7] The pre-combustion CO_2 capture/separation is more suited for integrated gasification combined cycle (IGCC) power plants where CO_2 is separated from a mixture of CO_2 and H_2 to allow final combustion to take place in pure H_2. The CO_2 concentration in an industrial pre-combustion stream of CO_2 and H_2 mixture typically ranges from 15 to 50%.[8] The post-combustion and oxygen-combustion captures are more applicable to conventional pulverized coal-fired (PC) and natural gas-fired power plants where CO_2 is separated from N_2-concentrated flue gas after fossil fuels are combusted in air.[3,9] The existing state-of-the-art CO_2 capture technologies mainly rely upon chemical/physical absorptions by liquid solvents or solid sorbents,[10–12] and are yet ready for commercial use at the larger scale necessary for power plant application. The parasitic loads (steam and power) required to support post-combustion CO_2 capture would decrease power generation capacity of the power plant by nearly one-third and increase levelized cost-of-electricity (COE) by as much as 80%.[13,14] Nevertheless, the ad-/absorption based CO_2 capture processes are still the mainstream technologies currently being actively optimized to meet the requirements for lowering energy penalty and COE.

In comparison to solvent- and sorbent-based CO_2 capture, membrane-based separation/capture technologies present cost advantages when applied to pre- and post-combustion CO_2 capture: no steam or chemical load, delivering high-pressure CO_2 and driving CO shifting reaction to completion.[15–19] However, the major challenges are the limited selectivity, thus product purity, and poor compatibility with high-temperature process stream. Therefore, developing an alternative high-temperature membrane technology to separate/capture CO_2 more selectively and efficiently for existing power plants is in great demand.

One category of gas separation membranes that has the potential to meet these requirements is the mixed ionic and electronic conductors.[20–25] Different from its absorption and size-exclusion rivals, the ionic transport membrane only allows the electrochemically active species to transport through the membrane under a gradient of electrochemical potential. Thereby, its selectivity is exclusive. Since this type of membrane normally operates at elevated temperatures in a continuous fashion, it also has an excellent compatibility with the high-temperature process stream. The best example of this kind of membrane is the oxygen transport membrane, or OTM, which has been developed for producing pure oxygen and synthetic gas at commercial scale. The key feature of OTMs is the high oxygen flux enabled by internal concomitant fast oxide-ion and electronic transport, which leads to a much simpler and more energy efficient reactor design compared to electrical oxygen pumps. Applying this principle to the membrane of selective CO_2 separation, two types of mixed conductors can be envisioned: (1) mixed carbonate-ion and oxide-ion conductor (MOCC) and (2) mixed carbonate-ion and electron conductor (MECC). These selective CO_2 separation membranes should be technically and economically more attractive than conventional electrically driven, molten carbonate fuel cell based CO_2 concentrators since no external electronics are needed.[26–28] Fig. 1 shows the working principles of these two membranes along with CO_2-separation enabling surface reactions. Based on these fundamental reactions, it is evident that MOCC is more suitable for CO_2 separation from a reducing stream such as CO_2 + H_2 where the electrochemical gradients of CO_3^{2-} and O^{2-} exist in the opposite direction across the membrane, *i.e.*, CO_3^{2-} is charge-balanced by O^{2-} inside the membrane. On the other hand, MECC is more adequate for CO_2 separation from an oxidizing stream such as flue gas (CO_2, O_2, and N_2) where the electrochemical gradients of CO_3^{2-} and e^- exist in the opposite direction across the membrane, *i.e.*, CO_3^{2-} is charge-balanced by e^- inside the membrane. In this case, both CO_2 and O_2 will permeate through the membrane, the mixture of which has been suggested to either recycle back to the combustion chamber for oxy-combustion[6] or convert into a pure stream of CO_2 and H_2O by combusting in a fuel (*e.g.*, syngas) as shown in Fig. 1(b).[29] The latter concept has been theoretically analyzed with the consideration of utilizing the substantial waste heat produced from the heavily exothermic fuel oxidation reactions as depicted in Fig. 1(b) to generate steam for electricity. The model clearly suggests that a fossil-fueled power plant using this process would consume only 12% more fuel per unit electricity produced than a power plant with no CO_2 capture system,[29] demonstrating the potential to meet U.S. DOE's goal that deployment of a CO_2 capture system at a fossil-fueled power plant should not increase the cost of electricity from the combined facility by more than 30%. Toward developing such an enabling membrane, we have recently reported for the first time a new MECC consisting of silver and molten carbonate (MC) with the highest CO_2 flux density reported among the other incumbent MECC systems.[30]

The work presented in this paper describes a study aimed at developing a robust, selective and efficient high flux dual-phase MOCC membrane as depicted in Fig. 1(a) for pre-combustion CO_2 capture. Dual-phase MOCCs represent a newer class of electrochemical CO_2 separation membranes, and have only been reported in a few systems such as LSCF (Sr- and Co-doped $LaFeO_3$) + MC,[22] YSZ (Y_2O_3-doped ZrO_2) + MC and GDC (Gd_2O_3-doped CeO_2) + MC.[23,24] The CO_2 permeance of these systems is typically in the order of 10^{-9} to 10^{-11} mole m^{-2} s^{-1} Pa^{-1} at 650 °C,[22–24] significantly lower than the target value of 1 sccm cm^{-2} for any potential commercial use. One of the reasons for the low permeance can be ascribed to the "inefficient" microstructure containing poorly intra- and interconnected phases that impede ionic transport. To demonstrate the important role played by microstructural features, we report in this study the use of a combined "co-precipitation" and "sacrificial template" method to synthesize a solid oxide porous matrix with highly interconnected solid and uniformly distributed pores. The molten carbonate phase then fills into these pores to form a dense MOCC membrane. Thus fabricated MOCC membranes exhibit the highest CO_2 flux density among the similar MOCC systems reported in the literature.

Experimental section

Synthesis of dual-phase ceramic-carbonate MOCC membranes

A two-step approach was employed to synthesize the dual-phase ceramic-carbonate MOCC membrane. The solid oxide phase $Ce_{0.8}Sm_{0.2}O_{1.9}$ (SDC) powder was first co-precipitated with NiO

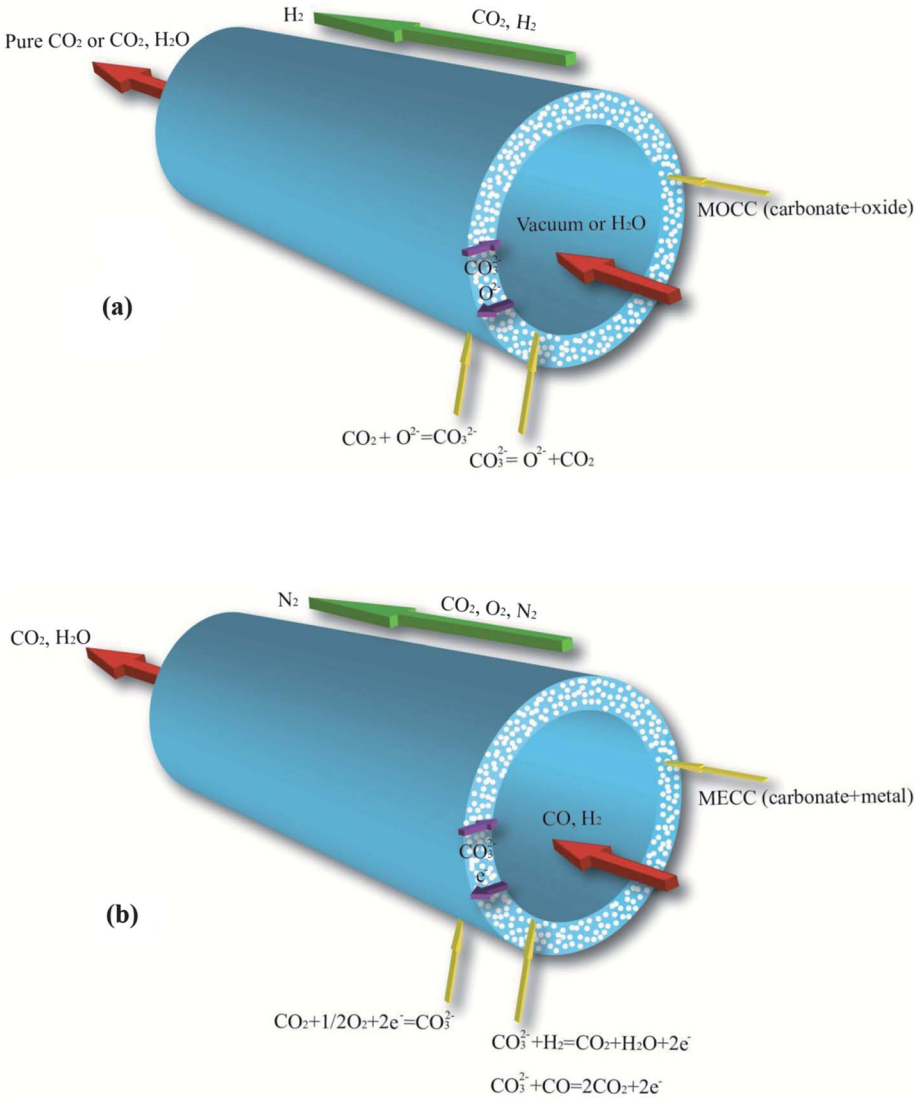

Fig. 1 Working principles of selective electrochemical CO_2 separation membranes: (a) MOCC and (b) MECC.

from the nitrates of the constituents using $(NH_4)_2CO_3$ as the mineralizer to form a uniformly distributed nanoscale particle composite. The NiO serves as the sacrificial phase. The molecular-level mixing ensures the highest degree of compositional homogeneity and phase interconnectivity. The details about the co-precipitation procedure are given in our recent publications.[31,32] The volume ratio between SDC and NiO was controlled to be in the range of SDC : NiO = 70 : 30 to 50 : 50, in which the volume fraction of NiO is equivalent to the ultimate porosity after the NiO phase is removed. The co-precipitated nanocomposite powders were then pressed into ϕ 25 mm pellets and sintered at 1400 °C in air for 2 hours. The well-sintered pellets were then reduced in pure H_2 at 800 °C for 10 h to convert nickel oxide to Ni metal. The Ni in the reduced composite was finally leached out by a 2.2 M nitric acid solution held at 80 °C for 24 h. The final thickness of the membrane is 1.2 mm.

The final dual-phase MOCC membrane was fabricated by filling pores in the SDC matrix with a carbonate melt of Li_2CO_3 and Na_2CO_3 (52 : 48 in mol%). The procedure can be briefly described as follows. The porous SDC pellet suspended in a silver wire is slowly immersed into the carbonate melt at 700 °C. After soaking for 4 hours, the temperature is ramped down. At 500 °C, a temperature slightly higher than the solidification temperature for MC (~495 °C), the MC-saturated SDC is slowly pulled out from the MC melt and hung over the melt as the furnace is continually cooled down to 100 °C when the sample is removed. The surface of the dual-phase membrane is finally polished using sandpaper with ethanol as a medium to remove the residual molten carbonate, followed by gas tightness check using a homemade leakage check device before it is assembled into a permeation cell.

CO_2 flux measurement

The CO_2 permeation characteristics of the synthesized MOCC were studied using a homemade permeation cell system, the configuration of which is schematically shown in Fig. 2. The MOCC pellet membrane was first sealed to a supporting alumina

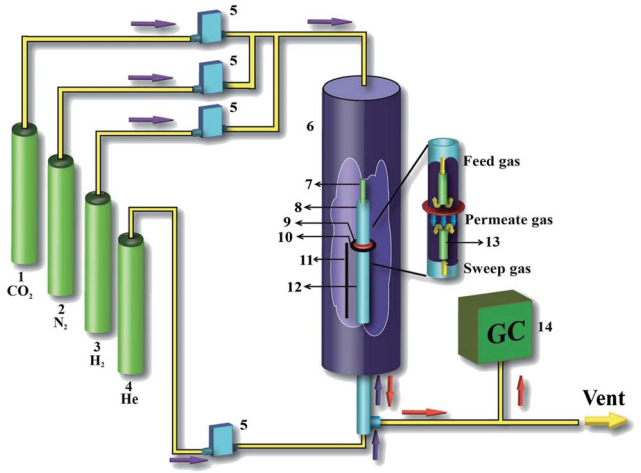

Fig. 2 Schematic of the CO_2 permeation cell configurations. (1) CO_2 cylinder; (2) nitrogen cylinder; (3) hydrogen cylinder; (4) helium cylinder; (5) mass flow controllers; (6) furnace; (7) inner feed tube; (8) second short alumina tube; (9) MOCC membrane; (10) sealant; (11) thermocouple; (12) supporting alumina tube; (13) inner sweep tube; and (14) gas chromatography (GC).

tube using a modified sealant containing a mixture of ceramic cement (Ceramabond 552-VFG, Aremco Products) and a commercial glass powder (Schott glass GM31107). A second short alumina tube was then bonded to the top of the sample for the purpose of shielding the feed gas. The assembly was cured at room temperature for 1–4 hours and 93 °C for a minimum of 4 hours before further raising the temperature. The feed gas was typically a mixture of 5 ml min^{-1} H_2, 50 ml min^{-1} CO_2 and 50 ml min^{-1} N_2; N_2 was used as a tracer gas for leak correction if any. A small amount of H_2 (4.8%) was added to the feed gas to lower the partial pressure of oxygen (P_{O_2}) so as to promote O^{2-} transport. For the study of H_2-effect on CO_2 flux density, a small increment in the flow rate of H_2 was simply added without changing the flow rates of CO_2 and N_2. The CO_2 permeated through the MOCC was swept from the surface of the permeate side by a high-purity helium (99.999%), at a flow rate of 50 ml min^{-1}, not by H_2O or vacuum as depicted in Fig. 1(b), for the purpose of convenient analysis of CO_2 concentration by an on-line micro-GC (Varian 490-GC, Varian). To ensure the data accuracy, the GC was calibrated with three standard gas compositions for each gas of interest (CO_2, O_2, and N_2). The concentration of CO_2 measured typically varies from 0.1% to 3.2% depending on the samples and actual testing conditions. The final CO_2 flux density was calculated out from an averaged gas composition of a total of ten successive readings from the GC. For all gas flows, commercial mass flow controllers (Smart-Trak, 50 Series) specifically calibrated for the gas under use were employed to control the mass flow rates. The temperature of permeation cells was varied from 550 to 700 °C in an interval of 25 °C. At each temperature, 30 minutes were given to allow the cell to reach a steady state before sampling. The concentration of N_2 in the sweeping gas was typically found to be low (<0.05%) for all measurements, which leads to a perm-selectivity in the range of 155–255, indicating that gas seals were not a major concern for this study. The level of leakage was also estimated, causing roughly 2% uncertainty in the final CO_2 flux density determination. Finally, the backpressure during CO_2 flux measurement could also potentially impact the CO_2 flux measured. In this study, it was constantly monitored during measurements, and found to be in the range of 1–2 psi; this level of backpressure is expected to have a little effect on the permeated CO_2 flux.

The flux densities of CO_2 and N_2 (leakage) were calculated using the following equations:

$$J_{N_2,\text{leak}} = \frac{c_{N_2}}{(1 - c_{CO_2} - c_{N_2})} \times \frac{Q}{S} \quad (1)$$

$$J_{CO_2,\text{total}} = \frac{c_{CO_2}}{(1 - c_{CO_2} - c_{N_2})} \times \frac{Q}{S} \quad (2)$$

where, c_{N_2} and c_{CO_2} are the measured concentrations of N_2 (leakage) and CO_2, respectively. Q (ml min^{-1}) is the flow rate of the helium sweeping gas, and S is the effective reaction area of the sample, 0.921 cm^2 for this study. The final leakage-corrected CO_2 flux density was calculated by

$$J_{CO_2} = J_{CO_2,\text{total}} - 1.0 \times J_{N_2,\text{leak}} \quad (3)$$

where the correction factor of 1.0 is the ratio between the CO_2 flow rate (50 ml min^{-1}) and N_2 flow rate (50 ml min^{-1}) in the feed gas.

Other characterization

The pore characteristics of the porous SDC including pore size distribution, median pore diameter, porosity and tortuosity were obtained by a mercury porosimeter (Autopore IV, Micromeritics) in a pressure range of 0.5–30 000 psi. The two-dimensional (2D) microstructural features and elemental distributions of the porous SDC matrix as well as MC-filled MOCC membrane were captured and analyzed by a field emission scanning electron microscope (FESEM, Zeiss Ultra) equipped with an energy dispersive X-ray spectroscopy (EDS) analyzer.

The three-dimensional (3D) microstructure of the porous SDC was obtained by reconstructing transmission images acquired using a synchrotron-based transmission X-ray microscope.[33] A sample suitable for use in such X-ray nanotomography measurements was first created using a FIB-SEM milling technique.[34] A cylinder approximately 10 microns in diameter and 20 microns in length was extracted from the bulk material and attached vertically on the tip of a pin. The sample was then mounted in the transmission X-ray microscope at the National Synchrotron Light Source beamline X8C in Brookhaven National Laboratory. X-ray nanotomography was performed at 8365 eV by rotating the sample between −90° and +90° in 0.5° increments, which produces images with a zone plate spatial resolution of roughly 30 nm. Images of the sample were taken at each angular position with an exposure time of 10 seconds per image and a spatial resolution of 30 nm as dictated by the zone plate characteristics.[33] The tomography dataset was reconstructed using a filtered back projection algorithm to obtain a 3D volumetric representation of the sample. The phase size distributions (PSD) were calculated using a ray-shooting method based on the imaged structure obtained from X-ray nanotomography. A detailed description on image analysis can be

found in ref. 33–36. The important microstructural features such as phase volume fraction, phase size distribution (PSD), contiguity, and interfacial contact area per unit volume can be obtained from the analysis.

Results and discussion

The reconstructed 3D microstructure of a SDC50 (50 vol% SDC) porous matrix by X-ray nanotomography shown in Fig. 3(a) can be generally characterized as a sponge-like framework with excellent intra- and interconnectivity between the SDC matrix and pores. Subsequent image analysis of two Representative Volume Elements (RVEs) reveals a 100% contiguity of each individual phase (pore, SDC), 54% pore volume fraction and 46% SDC volume fraction. The number-weighted mean pore size and the number-weighted mean SDC phase size are 609 nm and 485 nm, respectively, as shown in Fig. 3(b). The interfacial contact area between the pores and SDC phase per unit volume was measured to be 5.7 $\mu m^2\ \mu m^{-3}$. These microstructural parameters suggest the fabricated SDC as a highly and efficiently interconnected porous network. A regular FESEM image shown in Fig. 3(c) illustrates a similar microstructural feature in 2D fashion: uniform distributions of pore and SDC. The pore size is estimated to be ~550 nm, fairly close to that determined from X-ray nanotomography. The mercury porosimetry data shown in Fig. 3(d) indicate a median pore size of 600 nm and a porosity of 50.2%, both of which are also in reasonably good agreement with those obtained from 3D X-ray nanotomography and 2D SEM. A summary of all the microstructural features of the porous SDC obtained by these three techniques is given in Table 1.

Table 1 Summary of microstructural parameters of SDC50 (50 vol% SDC) obtained from X-ray nanotomography, FESEM and mercury porosimetry[a]

		X-ray nano-CT	FESEM	Mercury porosimetry
Volume fraction	Pore	54%	—	50.2%
	SDC	46%	—	49.8%
Mean pore size (nm)		609	550	600
Mean SDC size (nm)		485	—	—
Contiguity	Pore	100%	—	—
	SDC	100%	—	—
Interface contact area per unit volume ($\mu m^2\ \mu m^{-3}$)		5.75	—	—

[a] Calculated using pore volume fraction.

The microstructure and chemical elemental distributions of the prepared MOCC membrane are illustrated in Fig. 4. The glassy phase shown in Fig. 4(a) represents the MC whereas the grain-like lighter phase is the SDC phase. Evidently, the overall MOCC possesses a dense microstructure with the MC phase completely filling the porous SDC matrix. Thus formed dense microstructure ensures that the permeated CO_2 directly resulted from the concomitant transport of CO_3^{2-} and O^{2-}, not from free CO_2 molecules. The chemical homogeneity indicated by EDX mapping of constituent elements in Fig. 4(b)–(d) also supports that the SDC and MC phases are well distributed and homogeneously mixed across the membrane.

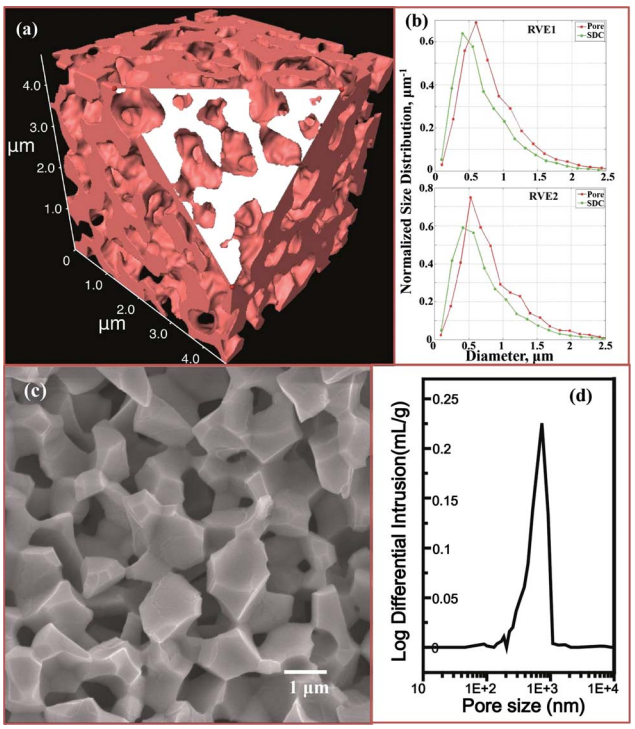

Fig. 3 Microstructural features of a SDC50 (50 vol% SDC). (a) Reconstructed 3D microstructure and (b) pore and phase size distributions of two RVEs (Representative Volume Elements) obtained by X-ray nanotomography; (c) SEM 2D microstructure; and (d) pore size distribution obtained by mercury porosimetry.

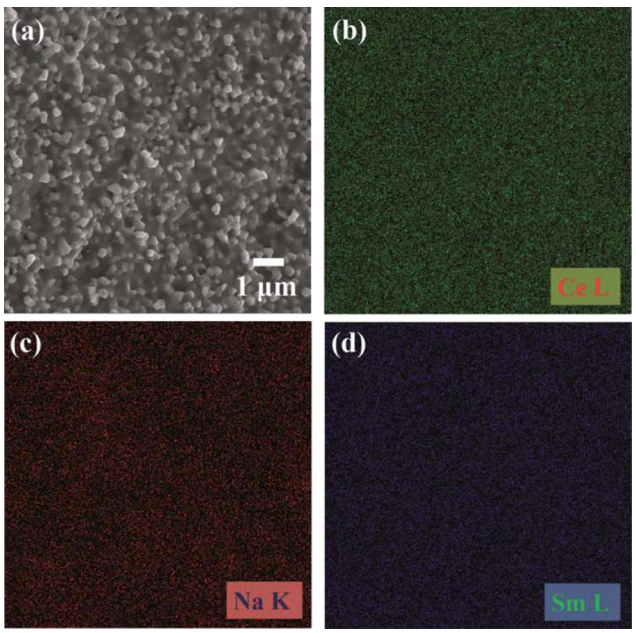

Fig. 4 Microstructure and elemental distributions of a MOCC based on a SDC60 (60 vol% SDC) porous matrix. (a) FESEM image; (b) Ce mapping; (c) Na mapping; and (d) Sm mapping. *Note*: Li is too light to be detected by EDX.

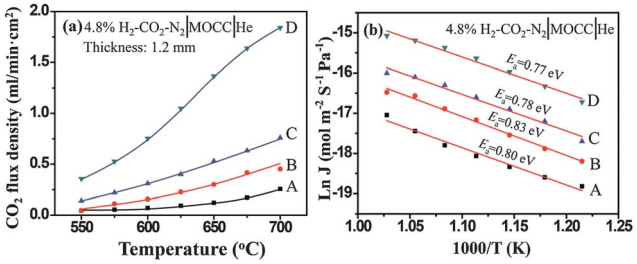

Fig. 5 (a) CO_2 flux density as a function of temperature and (b) Arrhenius plots of CO_2 flux density. MOCC-A: 70 vol% SDC–30 vol% MC; B: 65 vol% SDC–35 vol% MC; C: 60 vol% SDC60–40 vol% MC; and D: 50 vol% SDC–50 vol% MC.

The CO_2 flux densities measured from a series of MOCC compositions are shown in Fig. 5 as a function of temperature. As expected, the CO_2 flux densities increase with temperature, confirming that the transport of CO_3^{2-} and O^{2-} is a thermally activated process. For a given temperature, the CO_2 flux densities also increase with the volume fraction of the MC phase, which can be ascribed to a combined effect from microstructural factors, volume fractions and conductivity of each phase. This trend is also favorably confirmed by the theoretical analysis of ionic transport to be discussed later. Overall, the level of CO_2 flux density achieved is remarkable: at 700 °C the level of flux density increases from 0.26, 0.45, 0.64 to 1.84 ml min^{-1} cm^{-2} for MOCC-A (30 vol% MC) through D (50 vol% MC), respectively. The high flux promises the lowering of operating temperature, particularly when thinner membranes are employed, to enhance the durability for potential commercial applications.

The CO_2 flux densities are also observed to follow closely with the Arrhenius relationship in Fig. 5(b), the slope of which representing the activation energy, E_a, varies from 0.80, 0.83, 0.78 to 0.77 eV for MOCC-A through D, respectively. These values are sufficiently close to 0.78 eV for oxide-ion conduction in SDC electrolytes reported in the literature,[37] suggesting that the ionic transports in these samples share the same mechanism and are limited by the oxide-ion migration. Such an understanding is reasonable considering the fact that the conductivity of oxide-ions in the SDC phase is more than two orders of magnitude lower than that of the MC phase.

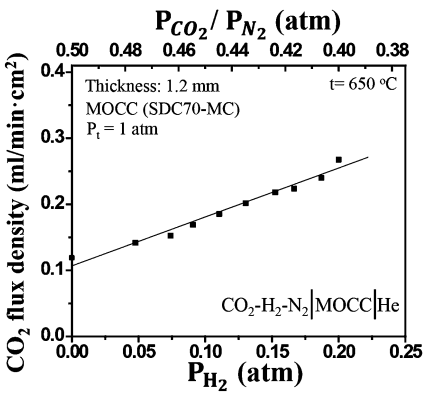

Fig. 6 Dependence of CO_2 flux density of MOCC-A on H_2-concentration at 650 °C.

The fact that the CO_2 flux density is limited by the oxide-ion transport is further confirmed in Fig. 6 where CO_2 flux density of MOCC-A (70 vol% SDC–30 vol% MC) is shown to linearly increase with partial pressure of hydrogen (P_{H_2}). An increased P_{H_2} implies a lowered P_{O_2}, which in turn increases the chemical gradient of oxygen across the membrane, thus raising the flux of oxide-ion. By the requirement of charge neutrality, the flux of carbonate-ion will be correspondingly enhanced. The sensitivity of CO_2 flux density to P_{H_2} is an indirect piece of evidence that the bulk oxide-ion transport is a flux-limiting step.

An important side chemical reaction worth investigating when dealing with the H_2 and CO_2 mixture is the carbon formation as a result of the reverse water gas shift reaction $CO_2 + H_2 = CO + H_2O$ and Boudouard reaction $2CO = CO_2 + C$. Thermodynamic analysis outlining the boundaries for carbon formation under the tested conditions is given in the ESI†. A general trend is that the temperature at which carbon is formed increases with P_{H_2}. To avoid coking, the minimum temperature for flux measurements carried out in this study was set to 550 °C.

The obtained CO_2 flux densities of the MOCC with various compositions are also compared with the literature in Fig. 7. To do so, the measured flux densities shown in Fig. 5(a) need to be converted into CO_2 permeability as defined by $J_{CO_2}/\Delta P_{CO_2}$ along with normalized thickness. The comparison indicates that the permeability of the MOCC developed in this study is at least two orders of magnitude higher than that reported in YSZ–MC and CGO–MC at 650 °C (ref. 23) and at least one order of magnitude higher than the LSCF–MC membrane at 700 °C.[22] The significant improvements are attributed to the highly efficient microstructure synthesized by the combined "co-precipitation" and "sacrificial template" method, which provides a vast number of intra- and interconnected ionic channels for high-rate ionic transport in dual phase mixed-ion conductors.

The CO_2 flux densities shown in Fig. 5(a) are also compared in Fig. 8 with theoretical calculations. The equation employed in the calculation has been derived from classical flux theory, but with additional consideration of microstructural and concentration factors as follows:

$$J_{CO_2} = -\left(\frac{\varepsilon}{\tau}\right)\frac{RT}{4F^2L}\,\frac{\varphi\sigma_c(1-\varphi)\sigma_o}{\varphi\sigma_c+(1-\varphi)\sigma_o}\ln\frac{P''_{CO_2}}{P'_{CO_2}} \qquad (4)$$

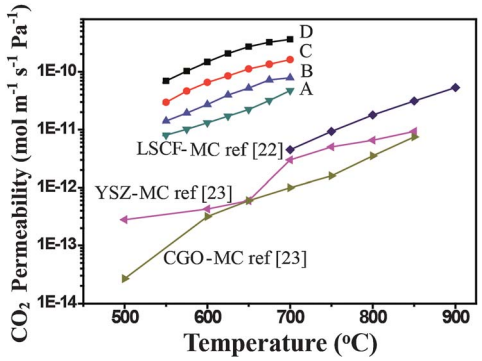

Fig. 7 Comparison of CO_2 permeability of the MOCC developed in this study with LSCF–MC, YSZ–MC and CGO–MC membranes available in the literature. Letters A through D have the same meanings as those in Fig. 5(a).

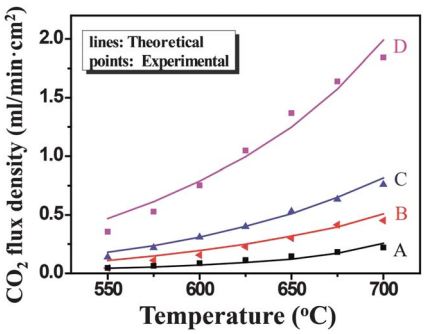

Fig. 8 Comparison of the measured CO_2 flux density with theoretical calculations using existing flux transport model. Letters A through D have the same meanings as those in Fig. 5(a).

where ε and τ are the porosity and the tortuosity of the porous SDC, respectively; R is the gas constant, 8.314 J mol^{-1} K^{-1}; T is the absolute temperature, K; F is Faraday's constant, 96 500 C mol^{-1}; L is the thickness of the membrane, cm; φ is the volume fraction of the MC phase; σ_c and σ_o are the conductivities of carbonate-ions and oxide-ions in S cm^{-1}, respectively; P'_{CO_2} and P''_{CO_2} are the partial pressures at the feed and permeate sides in Pa, respectively. A detailed derivation of eqn (4) can be found in the ESI†. The parameters used for the calculations are listed in Table 2, where the microstructural factors such as ε and τ are obtained directly from mercury porosimetry measurements. The independently calculated values are in excellent agreement with those independently measured values in Fig. 8, which convincingly validates the microstructure-modified flux eqn (4) and confirms that the ionic transport is controlled by bulk-diffusion of ions at the thickness level of this study.

The flux density measured in this study is usually stable during the characterizing period (10–15 hours). However, extended testing shows flux degradation accompanied by an increased concentration of N_2. Comparison of XRD patterns performed on samples before and after test indicates that the intensity of the MC phase in the post-test sample is significantly lower than that in the pre-test sample, implying that loss of the MC phase could be the reason for the degradation. Therefore, the retention of MC is critical to the long-term stability of the MOCC membrane. The knowledge to immobilize MC can be learned from molten carbonate fuel cell technology and is currently being applied to this ongoing research, the results of which will be reported in the near future.

Table 2 Parameters used in the calculations of theoretical CO_2 flux density

$\sigma_o = 224.6 \exp(-9051.5/T)$ $T = 400$–700 °C (S cm^{-1})[37]				
$\sigma_c = 83.8 \exp(-3716.7/T)$ $T = 450$–650 °C (S cm^{-1})[20]				
Thickness (mm)			1.2	
P'_{CO_2} (Pa)			48 250	
P''_{CO_2} (Pa)			Varied	
	φ	ε	τ	ε/τ
Sample A	0.30	0.321	26.1	0.0123
Sample B	0.40	0.366	11.3	0.0324
Sample C	0.45	0.436	5.71	0.0765
Sample D	0.50	0.531	2.27	0.234

Conclusions

A dual-phase mixed-ion conducting membrane for selective electrochemical CO_2 separation from a fuel gas stream has been successfully synthesized by filling a highly interconnected, porous solid oxide-ion conducting ceramic matrix with a carbonate-ion conducting molten carbonate. A combined "co-precipitation" and "sacrificial template" technique has been demonstrated to produce the highly efficient three-dimensional porous ceramic network containing a vast number of intra- and interconnected channels for fast ion transport. The performance of thus synthesized MOCC membrane is remarkable, showing a CO_2 flux density two orders of magnitude higher than the existing ceramic-carbonate systems fabricated with other methods. Moreover, the measured CO_2 flux densities are in excellent agreement with theoretical predictions derived from a microstructure-modified flux equation. Overall, the developed MOCCs show a great promise to be a new class of high-flux membranes for selective electrochemical separation of CO_2 from a pre-combustion process stream.

Acknowledgements

The authors of the University of South Carolina would like to thank DARPA (W91CRB-10-1-007) for the financial support. W.H. Harris and W.K.S. Chiu acknowledge financial support from an Energy Frontier Research Center on Science Based Nano-Structure Design and Synthesis of Heterogeneous Functional Materials for Energy Systems (HeteroFoaM Center) funded by the U.S. Department of Energy, Office of Science, Office of Basic Energy Sciences (award DE-SC0001061). Use of the National Synchrotron Light Source beamline 8XC (Jun Wang and Yu-Chen Chen), Brookhaven National Laboratory, was supported by the U.S. Department of Energy, Office of Science, Office of Basic Energy Sciences, under contract no. DE-AC02-98CH10886.

References

1 U. S. Energy Information Administration, *Energy Perspective 1949–2010*, October 19 2011.
2 U. S. Energy Information Administration, *Annual Energy Outlook 2011*, April 26, 2011.
3 DOE/NETL, *Carbon Dioxide Capture and Storage RD&D Roadmap*, December 2010.
4 DOE/NETL, *Advanced Carbon Dioxide Capture R&D Program: Technology Update*, September 2010.
5 R. Bredesen, K. Jordal and O. Bolland, *Chem. Eng. Process.*, 2004, **43**, 1129–1158.
6 B. J. P. Buhre, L. K. Elliott, C. D. Sheng, R. P. Cupta and T. F. Wall, *Prog. Energy Combust. Sci.*, 2005, **31**, 283–307.
7 M. O. Franklin, *Energy Environ. Sci.*, 2009, **2**, 449–458.
8 http://www.fossil.energy.gov/programs/sequestration/capture/.
9 E. Favre, *J. Membr. Sci.*, 2007, **294**, 50–59.
10 Y. Zhang and J. Y. G. Chan, *Energy Environ. Sci.*, 2010, **3**, 408–417.
11 S. Smart, C. X. C. Lin, L. Ding, K. Thambimuthu and J. C. D. da Costa, *Energy Environ. Sci.*, 2010, **3**, 268–278.
12 Q. Wang, J. Lou, Z. Zhong and A. Borgna, *Energy Environ. Sci.*, 2011, **4**, 42–55.
13 ARPA-E Carbon Capture Programs, *Taillores Post-Combustion Carbon Capture Workshop*, July 11 2010.
14 C. F. Hendricks, *Energy Environ.*, 1994, **1**, 19–49.
15 D. Shekhawal, D. R. Luebke and H. W. Pennline, DOE/NETL, 2003.
16 H. Kawamura, *et al.*, *J. Chem. Eng. Jpn.*, 2005, **38**(5), 322–328.
17 E. J. Granite and T. O'Brien, *Fuel Process. Technol.*, 2005, **86**, 1423–1434.

18 N. Du, H. B. Park, M. M. Dal-Cin and M. D. Guiver, *Energy Environ. Sci.*, 2012, **5**, 7306–7322.
19 J. D. Figueroa, T. Fout, S. Plasynski, H. McIlvried and R. D. Srivastava, *Int. J. Greenhouse Gas Control*, 2008, **2**, 9–20.
20 S. J. Chung, J. H. Park, D. Li, J.-I. Ida, J.-I. Kumakirix and Y. S. Lin, *Ind. Eng. Chem. Res.*, 2005, **44**, 7999–8006.
21 K. S. Lackner, A. C. West and J. L. Wade, WO2006113674, ed. U. Columbia, United States, 2006.
22 M. Anderson and Y. S. Lin, *J. Membr. Sci.*, 2010, **357**, 122–129.
23 J. L. Wade, C. Lee, A. C. West and K. S. Lackner, *J. Membr. Sci.*, 2011, **369**, 20–29.
24 J. L. Wade, K. S. Lackner and A. C. West, *Solid State Ionics*, 2007, **178**, 1530–1540.
25 Z. Rui, M. Anderson, Y. S. Lin and Y. Li, *J. Membr. Sci.*, 2009, **345**, 110–118.
26 J. L. Weaver and J. Winnick, *J. Electrochem. Soc.*, 1983, **130**(1), 20–28.
27 M. P. Kang and J. Winnick, *J. Appl. Electrochem.*, 1985, **15**, 431–439.
28 K. Sugiura, K. Takei, K. Tanimoto and Y. Miyazaki, *J. Power Sources*, 2003, **118**, 218–227.
29 S. Sherman, K. Brinkman, J. Gray and K. Huang, *J. Membr. Sci.*, 2012, **401–402**(5), 323–332.
30 N. Xu, X. Li, M. A. Franks, H. Zhao and K. Huang, *J. Membr. Sci.*, 2012, **401–402**(5), 190–194.
31 L. Zhang, Z. Mao, J. D. Thomason, S. Wang and K. Huang, *J. Am. Ceram. Soc.*, 2012, **95**(6), 1832–1837.
32 L. Zhang, X. Li, S. Wang, K. G. Romito and K. Huang, *Electrochem. Commun.*, 2011, **13**(6), 554–557.
33 K. N. Grew, Y. S. Chu, J. Yi, A. A. Peracchio, J. R. Izzo, F. Y. Hwu, F. De Carlo and W. K. S. Chiu, *J. Electrochem. Soc.*, 2010, **157**(6), B783–B792.
34 J. J. Lombardo, R. Ristau, W. H. Harris and W. K. S. Chiu, *J. Synchrotron Radiat.*, 2012, DOI: 10.1107/S0909049512027252, submitted.
35 K. N. Grew, A. A. Peracchio and W. K. S. Chiu, *J. Power Sources*, 2010, **195**, 7943–7958.
36 K. N. Grew, A. A. Peracchio, A. S. Joshi, J. R. Izzo and W. K. S. Chiu, *J. Power Sources*, 2010, **195**, 7930–7942.
37 T. Mori, Y. Wang, J. Drennan, G. Auchterlonie, J. G. Li and T. Ikegami, *Solid State Ionics*, 2004, **175**, 641–649.